Loss of PINK1 causes age-dependent mitochondrial trafficking deficits in nigrostriatal dopaminergic neurons through aberrant activation of p38 MAPK

Jingyu Zhao[1,2], Yuanxin Chen[2,3], Lianteng Zhi[2], Qing Xu[4], Hui Zhang[2,3 *], Chenjian Li[1*]

1. The MOE Key Laboratory of Cell Proliferation and Differentiation, School of Life Sciences, Peking University, Beijing, 100871, China
2. Department of Neuroscience, Thomas Jefferson University, Philadelphia, PA 19107, United States
3. Department of Physiology & Pharmacology, The University of Georgia, Athens, 30602, United States
4. Biological and Environmental Sciences and Engineering Division, King Abdullah University of Science and Technology, Saudi Arabia, Thuwal, 23955–6900, Kingdom of Saudi Arabia

*To whom correspondence should be addressed:

Corresponding Author:

Hui Zhang, PhD
Associate Professor
Center for Neurological Disease Research
Department of Physiology & Pharmacology
College of Veterinary Medicine
The University of Georgia
501 D.W. Brooks Drive
Athens, GA 30602
Email: Hui.Zhang1@UGA.edu

Chenjian Li, PhD
Professor
The MOE Key Laboratory of Cell Proliferation and Differentiation
School of Life Sciences, Peking University
Beijing, China, 100871
Email: li_chenjian@pku.edu.cn; cjli2020@stanford.edu

Abstract

Mutations in *PTEN-induced putative kinase 1* (*PINK1*) gene cause early-onset, autosomal-recessive familial inherited Parkinson's disease (PD). Previous studies have shown age-related declines in dopamine release and ATP levels in the striatum of *Pink1*$^{-/-}$ mice, but the underlying mechanisms remain unclear. While the role of PINK1 in mitochondrial transport has been studied in cell culture and *Drosophila*, its impacts on axonal transport in dopaminergic neurons and the consequent synaptic and axonal degeneration *in vivo* remain critical questions that warrant further investigation. In this study, we developed a TH-mito-Dendra2 transgenic mouse model to label mitochondria in dopaminergic neurons with Dendra2 protein. Using this model, we found that loss of PINK1 causes age-dependent deficits in mitochondrial axonal trafficking, with reduced anterograde movement and increased static mitochondria in acute brain slices. Inducing ROS and calcium release pharmacologically impaired mitochondrial motility, and *Pink1*$^{-/-}$ mice exhibited elevated mitochondrial calcium and ROS levels. Furthermore, *Pink1*$^{-/-}$mice showed p38 MAPK hyperactivation and reduced Miro1 expression. Treatment with the p38 inhibitor SB202190 restored mitochondrial motility and increased anterograde transport. Taken together, our findings suggest that loss of PINK1 disrupts mitochondrial trafficking by disturbing calcium homeostasis and ROS production via the p38 pathway for PD pathogenesis.

KEY WORDS: Parkinson's disease, PINK1, dopaminergic neurons, mitochondrial axonal transport, calcium homeostasis, oxidative stress, p38 MAPK

Introduction

Parkinson's disease (PD) is a major neurodegenerative disorder affecting people above 65 years old, characterized by dopamine neuron loss in the substantia nigra pars compacta (SNc) leading to striatal dopamine deficiency (Poewe et al., 2017). While the pathogenesis of PD is complex, mounting evidence implicates mitochondrial dysfunction as a key initiating factor (Malpartida et al., 2020). Mitochondrial abnormalities in PD include altered morphology, impaired energy production, increased oxidative stress, dysregulated dynamics and calcium homeostasis, and disrupted mitophagy. However, it remains unclear whether these mitochondrial defects are primary causes or downstream consequences in PD. The identification of *PINK1* as a PD gene provided direct evidence linking mitochondrial dysfunction to PD pathogenesis (Winklhofer and Haass, 2010). PINK1 regulates key mitochondrial processes like mitophagy, calcium homeostasis, and fission in neurons, underscoring its relevance in studying mitochondrial dysfunction's role in PD. PINK1 loss-of-function models demonstrate mitochondrial defects like increased fission (Pryde et al., 2016), depolarization (Exner et al., 2012), impaired electron transport chain complexes I and III (Park et al., 2018; Vilain et al., 2012), and calcium overload (Kostic et al., 2015). Additionally, PINK1 interacts with Miro/Milton, implicating its role in mitochondrial trafficking (Weihofen et al., 2009).

Neurons, especially synapses, are highly energy demanding. A human cortical neuron utilizes ~4.7 billion ATPs/second at rest (Zhu et al., 2012), underscoring the importance of mitochondrial trafficking. Following evidence that PINK1 can interact with trafficking adaptor proteins (Weihofen et al., 2009), several studies have explored the relationship between PINK1 and mitochondrial stand mitochondrial trafficking in different models. One study demonstrated that overexpression of PINK1 or Parkin in rat hippocampal axons significantly reduced mitochondrial motility. For impaired mitochondria, PINK1 phosphorylates Miro, leading to Parkin-dependent Miro degradation and subsequent dissociation of kinesin from mitochondria, thus sequestering depolarized mitochondria (Wang et al., 2011). Another study demonstrated that D-AKAP1/PKA (D-AKAP1, dual-specificity A Kinase Anchoring protein 1; PKA, Protein Kinase A) can restore the mitochondrial trafficking deficiency in cortical neurons from PINK1 knockout (KO) mice (Das Banerjee et al., 2017). While these studies support the critical role of PINK1/Parkin pathway in regulating mitochondrial trafficking (Sheng, 2014), most current research utilizes *in vitro* systems or *Drosophila* models, which differ from *in vivo* conditions.

Additionally, most studies are not specific to dopaminergic neurons. From this perspective, further investigations closer to *in vivo* settings and focused on dopaminergic neurons are needed.

Here, we generated a new Mito-Dendra tool mouse model to specifically label mitochondria in dopaminergic neurons and established a new approach to directly observe mitochondrial trafficking in nigrostriatal dopaminergic neurons in acute brain slices from a *Pink1*$^{-/-}$ mouse model. We found an age-dependent impairment of mitochondrial motility and anterograde transport in dopaminergic neurons lacking PINK1 mediated through the aberrant p38 pathway. These results provide a possible explanation for our previous findings of decreased dopamine release and ATP production in the striatum of middle-aged *Pink1*$^{-/-}$ mice (Zhi et al., 2019).

Results

Generation and characterization of TH-MitoDendra2 BAC transgenic mice

To specifically label mitochondria in dopaminergic neurons, we generated a bacterial artificial chromosome (BAC) clone encompassing the entire tyrosine hydroxylase (*Th*) gene (Figure 1A). A mitochondria-targeting photo-convertible fluorescent protein Dendra2 gene (Gong et al., 2002; Wang et al., 2008) was inserted in the *Th* exon 1 (Figure 1A). The co-localization of mito-Dendra2 and the immunofluorescence for TH confirmed the specificity of mito-Dendra2 in dopaminergic neurons within the SNc and ventral tegmental (VTA) area (Figure 1B-1E). We also verified the specificity of Mito-Dendra2 signals at the dopaminergic terminals in the striatum and olfactory bulb (Figure S1) and the results showed mito-Dendra2 only expressed in TH positive neurons and neurites. Moreover, the co-localization of mito-Dendra2 signals with MitoTracker staining verified the subcellular localization of mito-Dentra2 in mitochondria (Figure 1F). Using this model, we can visualize the continuous and intact projection bundles from dopaminergic neurons in the SNc to the striatum in the sagittal view (Figure 1E, S2). These results demonstrate that mito-Dendra2 is specifically localized in the mitochondria of dopaminergic neurons and their projections, providing a novel and powerful tool for studying mitochondrial trafficking in these neurons.

Investigation of mitochondrial movement in acute brain slices with two-photon laser microscopy (2PLSM)

To evaluate mitochondrial trafficking in *Pink1*$^{-/-}$ mice, we crossed them with mito-Dendra2 transgenic mice to generate *Pink1*$^{-/-}$ /MD+ transgenic mice (Figure 2A). We chose to use acute sagittal brain slices (Figure 2A), which closely mimic *in vivo* conditions, to monitor mitochondrial trafficking. Two-photon laser scanning microscopy (2PLSM) was employed to track mitochondrial movement. Using time-lapse imaging, we visualized and recorded movies showing mitochondrial trafficking along the axon bundles (Figure 1E, Figure 2A, and B). Mitochondrial movement was primarily classified into three states: stationary, anterograde (moving towards the terminals), and retrograde (moving towards the cell body). As depicted in Figure 2B and Movie S1, we clearly captured mitochondrial movement at sequential time points. After collecting mitochondrial trafficking data, we used the software Fiji with two plugins, KymographDirect and KymographClear (Mangeol et al., 2016), to analyze the differences in the percentage and velocity of moving mitochondria (Figure 2C).

Age-dependent mitochondrial axonal transport deficits in *Pink1*$^{-/-}$ mice

After establishing the procedure, we evaluated the alterations in mitochondrial trafficking between *Pink1*$^{-/-}$ mice and age-matched wild-type (WT) littermates at different ages (Figure 3, Tables S1-S3). The percentages of stationary, anterograde, and retrograde mitochondria were similar in 2–4-month-old *Pink1*$^{-/-}$ mice and WT littermates (Figures 3A1-A2, 3B1-B2, 3C, Table S1). The average velocities of anterograde and retrograde movement were also comparable (Figure 3D, Table S1). Approximately 84-85% of mitochondria were stationary in both genotypes at 2-4 months, which is higher than typically reported in cultured cells (Schwarz, 2013; Sheng, 2014). In these mice, about 11% of mitochondria moved anterogradely and 4-5% moved retrogradely, differing from the more balanced 15% anterograde and 15% retrograde movement seen in cultured cells.

In 5-7-month-old *Pink1*$^{-/-}$ mice, the proportion of stationary mitochondria increased significantly from 85.18±0.64% to 90.79±0.69% ($p<0.0001$). Anterograde movement decreased from 9.95±0.94% to 5.63±0.77% ($p=0.0019$), while retrograde movement showed a slight decrease (Figures 3A3-A4, 3B3-B4, 3E, Table S2). Additionally, the anterograde velocity decreased significantly (0.52±0.02 μm/s, $p=0.0209$) (Figure 3F, Table S2). This reduction in anterograde movement may result in fewer mitochondria being transported to axonal terminals.

In *Pink1*$^{-/-}$ mice older than 10 months, the percentage of static mitochondria increased significantly to 91.72±1.07% compared to WT littermates (p=0.0251), while anterograde movement decreased to 2.18±0.55% (p=0.0068) (Figures 3A5-A6, 3B5-B6, 3G, Table S3). In these older *Pink1*$^{-/-}$ mice, retrograde mitochondrial transport exceeded anterograde transport, reaching 6.10±1.12% (Figure 3G, Table S3). Since retrograde-moving mitochondria are typically associated with damage (Schwarz, 2013), this suggests an increased proportion of dysfunctional mitochondria in middle-aged *Pink1*$^{-/-}$ mice. Furthermore, the anterograde velocity was significantly decreased to 0.34±0.03 µm/s (p=0.0018) compared to age-matched WT controls, while retrograde velocity remained unchanged (Figure 3H, Table S3).

In summary, *Pink1*$^{-/-}$ mice exhibited age-dependent deficits in mitochondrial axonal trafficking. These deficits, which were not present in 2-4 months old mice, emerged around 5 months of age and persisted beyond 10 months of age. The trafficking abnormalities included an increased proportion of static mitochondria, a decreased proportion of motile mitochondria, and slower anterograde mitochondrial velocities. These findings differ from previous reports in cultured neurons (Wang et al., 2011) and *Drosophila* (Liu et al., 2011), highlighting potential differences between *in vivo* and *in vitro* models, as well as between invertebrate and vertebrate systems.

Mitochondrial calcium elevation and transport deficits in *Pink1*$^{-/-}$ mice

Mitochondrial axonal transport is a tightly regulated process involving many factors. Cytosolic Ca^{2+} can modulate mitochondrial motility via the Miro protein (Wang and Schwarz, 2009). Furthermore, mitochondria themselves play a pivotal role in calcium homeostasis (Giorgi et al., 2018). However, the specific effect of mitochondrial calcium levels on mitochondrial motility remains unclear in the context of PINK1 deficiency in mice. To address this, we first evaluated mitochondrial calcium concentration in 2- to 4- months-old *Pink1*$^{-/-}$ mice using AAV9-TH-mito-GCaMP6, a modified GCaMP6 virus that is specifically expressed in mitochondria in dopaminergic neurons. Figure 4A and 4B show that the relative $[Ca^{2+}]_{mt}$ (relative fluorescence intensity) was significantly increased in *Pink1*$^{-/-}$ mice (78.61±4.28%) compared to WT littermates (35.69±4.61%). Next, we investigated the effect of elevated mitochondrial calcium on mitochondrial trafficking. We incubated WT acute brain slices with 5 µM CGP37157, an

inhibitor of the mitochondrial Na□/Ca²□ exchanger (NCLX) that causes mitochondrial calcium overload (Ruiz et al., 2014). Mitochondrial motility was significantly decreased after 2 hours of CGP37157 incubation (Figures 4C and 4D, Movies S2 and S3). The proportion of static mitochondria increased from 85.26±0.69% to 90.29±1.17% (p=0.0048), while anterograde movement declined from 8.69±1.07% to 5.62±0.85% (p=0.0432) (Figure 4D).

This phenomenon of altered mitochondrial motility following $[Ca^{2+}]_{mt}$ elevation was reminiscent of the findings observed in 5- to 7-month-old and above 10-month-old *Pink1*$^{-/-}$ mice, suggesting a similar underlying mechanism contributing to the mitochondrial trafficking defects in *Pink1*$^{-/-}$ mice. The velocities of anterograde and retrograde mitochondrial transport remained unaffected by the calcium perturbations in this experimental context (Figure 4E).

Reduced mitochondrial anterograde movement by ROS elevation

Mitochondrial calcium overload impairs normal mitochondrial function, leading to increased reactive oxygen species (ROS) generation and decreased ATP production (Peng and Jou, 2010; Santulli et al., 2015). To investigate whether elevated mitochondrial calcium levels result in increased ROS generation in acute brain slices, we used the mitochondrial NCLX inhibitor CGP37157 to induce mitochondrial calcium overload (Figure 5). Our results showed a significant increase in $[Ca^{2+}]_{mt}$, which led to an elevation in ROS levels (p=0.0005, Figure 5C). Subsequently, to investigate the impact of elevated ROS levels on mitochondrial trafficking dynamics, we exposed acute brain slice preparations from *WT* mice (5-7 months old) to 50 μM menadione (MED). Menadione is a widely employed compound known to exacerbate endogenous ROS production in cultured cell systems (Debattisti et al., 2017). Following a 20-minute incubation with 50 μM menadione, the proportion of stationary mitochondria significantly increased from 88.71±1.49% to 96.75±0.86% ($p < 0.0001$). Anterograde moving mitochondria were reduced by nearly 70%, from 6.70±1.14% to 2.20±0.73% ($p = 0.0189$), while retrograde movement also declined but did not reach statistical significance ($p = 0.0791$) (Figure 6A, 6B, and 6C, Movies S4 and S6). The average velocity of both anterograde and retrograde movement remained unchanged after MED treatment (Figure 6D). To rule out the possibility that decreased motility was due to DMSO toxicity, we also evaluated the effect of DMSO treatment on mitochondrial trafficking. The results showed no significant change in the percentage of

moving mitochondria and their velocity between ACSF control and DMSO treatment (Figure 6C and 6D, Movies S4 and S5). Additionally, we examined the effect of H_2O_2 treatment, another reagent commonly used to induce ROS generation, and observed similar results on mitochondrial trafficking (data not shown). These findings suggest that artificially increasing endogenous ROS levels in WT brain slices can impair mitochondrial motility, particularly affecting anterograde movement, similar to the deficits observed in *Pink1*$^{-/-}$ mice. We then evaluated ROS levels in *Pink1*$^{-/-}$ mice. Manganese superoxide dismutase (MnSOD), a crucial mitochondrial antioxidant enzyme, detoxifies oxygen free radicals generated during mitochondrial respiration. Evidence indicates that oxidative stress significantly upregulates MnSOD expression levels (Candas and Li, 2014). We quantified MnSOD expression levels in the striatum and SNc regions of *Pink1*$^{-/-}$ mice and WT littermates. Western blot analysis revealed a significant upregulation of MnSOD protein levels in 5–7-month-old *Pink1*$^{-/-}$ mice compared to WT littermates in both the striatum and nigrostriatal regions (Figure 6E and 6F), with an approximate 2-fold increase in striatal MnSOD expression (20.70±1.78 *vs.* 9.80±1.07) and a 1.75-fold elevation in the SNc region (9.59±1.51 *vs.* 3.48±0.97). Complementary immunofluorescence staining corroborated these findings, showing significantly higher MnSOD immunoreactivity in dopaminergic neurons from *Pink1*$^{-/-}$ mice compared to WT controls (Figure 6H and 6I). Quantitative analysis revealed an approximate 4-fold increase in relative MnSOD fluorescence intensity in *Pink1*$^{-/-}$ mice (3.69±0.30 *vs.* 1.00±0.08, $p<0.0001$). Collectively, these data provide compelling evidence for elevated oxidative levels in PINK1 knockout mice. The excessive ROS generation in acute brain slices from WT mice induced by menadione treatment was associated with impaired mitochondrial motility. These findings underscore a potential pathogenic link between PINK1-mediated mitochondrial dysfunction, dysregulated redox homeostasis, and disrupted mitochondrial trafficking, which may contribute to the degeneration of dopaminergic neurons in PD.

p38 MAPK pathway hyperactivation by loss of PINK1

We have already demonstrated that the of PINK1 causes mitochondrial calcium overload in dopaminergic neurons, resulting in a significant increase in intracellular ROS levels. Excessive ROS could lead to defects in mitochondrial axonal transport. However, the specific mechanisms by which excessive ROS affect mitochondrial movement in neurons remain to be fully elucidated. Previous studies have shown that intracellular ROS can inhibit the function of the

motor-adaptor complex that regulates mitochondrial motility through p38α MAPK pathway, thus reducing mitochondrial motility *in vitro* (Debattisti et al., 2017).

We then analyzed p38 phosphorylation level in *Pink1*$^{-/-}$ mice (6-7 months old) (Figure 7A and 7B). Immunoblot results showed that p38 phosphorylation levels were approximately threefold higher in *Pink1*$^{-/-}$ mice than in WT mice in the striatum (0.62±0.03 *vs.* 0.21±0.01, $p<0.0001$). The SNc region exhibited a similar increase in p38 phosphorylation levels (0.90±0.18 *vs.* 0.22±0.03, $p=0.005$). Elevated p38 phosphorylation indicates heightened activation of the p38 pathway. Collectively, these results suggest hyperactivation of the p38 MAPK pathway in *Pink1*$^{-/-}$ mice.

We extended our analysis to examine the phosphorylation levels of two other MAPK family pathways: JNK (Figure S3) and ERK (Figure S4). Our findings revealed that JNK phosphorylation levels were also elevated in *Pink1*$^{-/-}$ mice, while ERK phosphorylation levels remained unchanged. Both p38 and JNK pathways play crucial roles in cellular stress responses. The observed hyperactivation of these pathways in *Pink1*$^{-/-}$ mice further corroborates our earlier findings, indicating heightened oxidative stress in these animals. This aligns with our previous results and provides additional support for the oxidative stress hypothesis in PINK1 deficiency (Figure 6).

We also analyzed the protein expression involved in axonal mitochondrial transport (Figure S5). The adaptor protein Miro1 showed a significant reduction in *Pink1*$^{-/-}$ mice compared to WT littermates: approximately a 15% decrease in the striatum ($p=0.0263$) and approximately a 24% in the SNc ($p=0.0238$). This reduction in Miro1 may lead to decreased mitochondrial attachment to microtubules and reduced motility. However, we observed no significant changes in the expression of the motor proteins kinesin and dynein in *Pink1*$^{-/-}$ mice.

Improved mitochondrial motility in *Pink1*$^{-/-}$ mice by p38 inhibition

To validate whether inhibiting p38 activity could alleviate mitochondrial trafficking deficits in *Pink1*$^{-/-}$ mice, we treated acute brain slices from these mice with the p38 inhibitor SB202190 (Figure 7C-7F). Incubating *Pink1*$^{-/-}$ mice brain slices in ACSF containing 50 μM SB202190 for one hour significantly increased mitochondrial motility in dopaminergic neurons (Figure 7E).

The proportion of immobile mitochondria decreased from 90.93±0.51% to 84.59±0.61% ($p<0.0001$). The percentage of anterograde-moving mitochondria significantly increased from 4.96±0.86% to 11.12±1.36% ($p=0.0037$). Retrograde mitochondrial movement was not significantly affected (Ctrl.: 4.11±0.78% vs. SB202190: 4.29±1.15%). Additionally, SB202190 treatment did not alter the velocity of either anterograde or retrograde mitochondrial movement (Figure 7F).

We also verified the effectiveness of SB202190 treatment in *Pink1*$^{-/-}$ mice through immunoblot analysis, which showed a significant ~62% reduction in p38 phosphorylation (Figure S6). This substantial decrease in p38 phosphorylation led to a significant rescue of mitochondrial motility defects in dopaminergic neurons of *Pink1*$^{-/-}$ mice, particularly by increasing the percentage of anterograde movement. However, SB202190 treatment did not improve the decreased anterograde velocity in *Pink1*$^{-/-}$ mice.

Defective Mitochondrial quantity and quality in dopamine neuron terminals in *Pink1*$^{-/-}$ mice

Pink1$^{-/-}$ mice exhibited age-dependent deficits in striatal dopamine release and ATP levels (Zhi et al., 2019). This observation, along with the impaired mitochondrial axonal transport in *Pink1*$^{-/-}$ dopaminergic neurons, led us to hypothesize that reduced anterograde movement of mitochondria in *Pink1*$^{-/-}$ dopaminergic neurons might result in a depletion of healthy mitochondria at their axon terminals. To test this hypothesis, we employed tyrosine hydroxylase (TH) immunogold electron microscopy to directly assess mitochondrial morphology and quantify mitochondrial numbers. In WT mice (8-9 months old), dopaminergic neurons exhibited relatively intact mitochondrial cristae, indicating overall healthy mitochondria (Figure 8A). In contrast, *Pink1*$^{-/-}$ mice displayed notable mitochondrial abnormalities, including rounded mitochondrial shapes, indistinct cristae, and vacuolated internal structures, suggesting mitochondrial fragmentation (Figure 8B). The proportion of healthy mitochondria in dopaminergic terminals was significantly reduced in *Pink1*$^{-/-}$ mice (Figure 8C, 46.00±2.70% *vs.* 66.80±1.93%, $p=0.0088$). However, there was no significant change in the morphology of the total mitochondria in the striatum (Figure 8C, *Pink1*$^{+/+}$: 68.00±2.55% *vs.* *Pink1*$^{-/-}$: 71.40±4.16%). Compared with WT mice, the aspect ratio of mitochondria in the dopaminergic neurons of *Pink1*$^{-/-}$ mice was significantly reduced (*Pink1*$^{+/+}$: 3.13±0.23 *vs.* *Pink1*$^{-/-}$: 2.14±0.16, $p=0.0001$), indicating that the mitochondria at the terminals of dopaminergic neurons in *Pink1*$^{-/-}$ mice tended to be more rounded.

Taken together, our findings indicate that the loss of PINK1 leads to a significant increase in mitochondrial calcium levels in the SNc dopaminergic neurons by disrupting specific regulatory mechanisms. This disturbance in mitochondrial calcium homeostasis results in increased oxidative stress and ROS production, activate the p38 signaling cascade. Previous studies have shown that p38 can directly phosphorylate kinesin heavy chains (KHCs), thereby inhibiting axonal transport (Berth and Lloyd, 2023; Brady and Morfini, 2017; Debattisti et al., 2017; Morfini et al., 2013; Padzik et al., 2016). Based on these observations, we propose a working model (Figure 8G): the increase in ROS caused by loss of PINK1 activates the p38 MAPK pathway, leading to p38-mediated phosphorylation of the anterograde motor protein KIF5. This phosphorylation disrupts the mitochondrial anterograde transport complex, reducing the percentage of mitochondria undergoing anterograde movement. Consequently, the decreased anterograde trafficking of mitochondria results in a lower quantity of healthy mitochondria at the terminals of dopaminergic neurons. This deficit may lead to a reduction in ATP content at the neuron terminals, causing an energetic shortfall and decreased in dopamine release.

Discussion

Here, we developed and validated a novel approach that synergistically combines Mito-Dendra2 mice, acute brain slice preparations, and 2PLSM to specifically investigate mitochondrial axonal transport within dopaminergic neurons. This strategy allowed us to robustly interrogate mitochondrial transport kinetics in an *ex vivo* setting that more accurately recapitulates the pathophysiological scenario of PD in dopaminergic neurons, owing to the following key advantages: (i) Cell-type specificity: We focused specifically on the nigrostriatal dopaminergic neurons, which are the right and most vulnerable neuronal population in PD pathogenesis. (ii) Preserved neuronal network: Utilization of acute brain slices from mice provides a more integrated and physiologically relevant neuronal network that closely mimics *in vivo* conditions. Notably, the relative thickness of these slices helps maintain the coherence of the neuronal circuitry, including interactions among neurons, astrocytes, and glial cells, for a considerable duration, despite potential mechanical damage from sectioning. (iii) Sustained neuronal functionality and pharmacological interventions: This approach not only preserves the intrinsic functional activity of dopaminergic neurons for an extended duration but also enables us to

perform pharmacological manipulations and assess their effects on neuronal function and mitochondrial dynamics within an integrated *ex vivo* system.

Using this method, we investigated the mitochondrial trafficking alteration in our previous reported *Pink1*$^{-/-}$ mice (Zhi et al., 2019). Our findings reveal that loss of PINK1 causes age-dependent mitochondrial trafficking impairments in dopaminergic neurons, reducing healthy mitochondrial presence at terminals and provides a plausible mechanistic explanation for our previous finding (Zhi et al., 2019). Corroborating our findings, previous studies have also demonstrated that genetic ablation of *Pink1* in mouse primary cortical and midbrain neurons led to a significant reduction in the proportion of mitochondria undergoing anterograde movement along dendrites (Das Banerjee et al., 2017). Interestingly, some studies investigating loss of PINK1 in different models or neuronal subtypes have reported contrasting findings. Researches in rat primary hippocampal and *Drosophila* demonstrated that PINK1 deficiency led to an increase in the proportion of motile mitochondria (Wang et al., 2011; Liu et al., 2012). These divergent findings suggest that the effects of PINK1 deficiency on mitochondrial dynamics are context-dependent, varying across species, cell types, and developmental stages. This underscores the critical need to elucidate the molecular mechanisms underlying the differential susceptibility of specific neuronal populations to ubiquitous genetic perturbations.

Regarding the underlying mechanism of these deficits, we observed elevated ROS levels and p38 hyperactivation in *Pink1*$^{-/-}$ mice. Pharmacological inhibition of p38 rescued mitochondrial motility. Previous studies have elucidated a potential mechanism for how p38 activation specifically impacts mitochondrial axonal transport dynamics. These investigations indicated that heightened p38 activity leads to an increase in the phosphorylation status of the KIF5 protein, a key component of the kinesin motor complex. Notably, this enhanced phosphorylation of KIF5 results in a reduced binding affinity for microtubules, without affecting the overall expression levels of the kinesin motor protein itself (Berth and Lloyd, 2023; Brady and Morfini, 2017; Debattisti et al., 2017; Morfini et al., 2013; Padzik et al., 2016). However further validation is still needed in *Pink1*$^{-/-}$ mice.

Collectively, our studies introduce a novel approach to specifically investigate mitochondrial trafficking dynamics within dopaminergic neurons in Parkinson's disease mouse models. Applying this approach to *Pink1*$^{-/-}$ mice, we observed a unique phenotype of mitochondrial trafficking in dopaminergic neurons that differed from previous findings. This method can be further refined and adapted for other disease contexts and animal models in future studies. By integrating this approach with various tool mouse models, it offers the potential to investigate the transport dynamics of diverse organelles or proteins beyond mitochondria in different cellular environments.

Materials and methods

1. **Animals**

   Mice were housed in a temperature and humidity controlled specific pathogen-free (SPF) facility under a 12-hr light/dark cycle schedule with food and water available ad libitum. Transgenic mice were bred with wild-type FVB/N mice (Taconic). All experimental protocols were approved by the Animal Care and Use Committees of Thomas Jefferson University, Peking University, and The University of Georgia.

1. **Construction, modification and confirmation of TH-MitoDendra2-BAC**

   BAC clone covering the entire tyrosine hydroxylase (*Th*) gene was obtained from GENSAT RPCI23-350E13 (http://genome.ucsc.edu/cgi-bin/hgTracks?clade=mammal&org=Mouse&db=mm9&position=RP23-350E13). Dendra2-SV40 polyA from Clontech pCMV vector was ligated with a mitochondrial targeting sequence (Wang et al., 2008). The mitochondrial targeting sequence (MTS) was from human subunit 8A of cytochrome c oxidase (COX8A) (mitochondrial targeting sequence:
   5'ATGTCCGTCCTGACGCCGCTGCTGCTGCGGGGCTTGACAGGCTCGGCCCGG
   CGGCTCCCAGTGCCGCGCGCCAAGATCCATTCGTTGGGGGATCCACCGGTCG
   CCACC3')
   Mito-Dentra2 was inserted to the exon1 of *Th* gene with homologous recombination. Homologous arms, A arm (642 bp) and B arm (538 bp), from the first exon of *Th* were ligated to 5' and 3' ends of the mito-Dendra2 cassette by PCR amplification respectively and inserted into the shuttle vector following the standard protocol (Gong et al., 2002). The shuttle vectors were introduced into the RP23-350E13 competent cells to construct the co-integrated BACs using electroporation. Recombinants were identified by chloramphenicol and ampicilin resistant selection followed by PCR analysis (Gong et al., 2002). Purified TH-MitoDendra2 BACs were used to generate TH-MitoDendra2 transgenic mice.

2. **TH-MitoDendra2-BAC transgenic mice**

TH-MitoDendra2-BACs were used for pronuclear injection in the Taconic FVB/NTac background. Founders and progeny carrying the TH-MitoDendra2 transgene were identified by PCR analysis of tail DNA and direct sequencing. The expression pattern of mito-Dendra2 was confirmed using TH immunofluorescence in TH-MitoDendra2-BAC transgenic mice, showing complete overlap of the mito-Dendra2 signal (green) with TH antibody staining (red). The transgenic mice were maintained by breeding with wild-type Taconic FVB/NTac mice.

3. Immunofluorescence

Mice were anesthetized with ketamine/xylazine (100 mg/10 mg per kg) and then perfused with ice-cold 4% paraformaldehyde in phosphate-buffered saline (PBS) and postfixed for 24 hours. Coronal sections, 30 μm thick, were obtained using a Thermo Scientific Microm HM550 Cryostat. Serial sections were collected into 10 wells, with each well containing every 10th section. Floating sections were stored in antifreeze buffer (30% glycerol and 30% ethylene glycol in PBS) at −20°C. The sections were stained with a polyclonal anti-tyrosine hydroxylase (TH) antibody (Millipore, MAB5280) at a 1:1000 dilution for 36 hours at 4°C, followed by incubation with a Dylight 594-conjugated secondary antibody (1:500, Life Technologies). Fluorescent images were captured using a Leica SP3800 laser scanning confocal microscope.

4. Acute sagittal slice preparation

Animals were anesthetized with either isoflurane (1–2%) or ketamine/xylazine (100 mg/10 mg per kg) and then underwent transcardiac perfusion with ice-cold, pre-oxygenated cutting solution containing (in mM): 125 NaCl, 2.5 KCl, 26 NaHCO3, 3.7 MgSO4, 0.3 KH2PO4, and 10 glucose, pH 7.4). The brains were immediately dissected out in cold, pre-oxygenated cutting solution. Sagittal nigrostriatal projection slices were sectioned at a thickness of 300 μm using a vibrating microtome (VT1200, Leica, Solms, Germany) with an angle of approximately 21º. The slices were then recovered in oxygenated artificial cerebrospinal fluid (ACSF) containing (in mM): ACSF, in mM, 125 NaCl, 2.5 KCl, 26 $NaHCO_3$, 2.4 $CaCl_2$, 1.3 $MgSO_4$, 0.3 KH_2PO_4, 10 glucose, 2 HEPES, pH7.4, at room temperature for > 30 minutes.

5. **Two-photon laser microscopy imaging of mitochondrial trafficking in brain slices**

Parasagittal slices containing nigrostriatal projections were obtained from TH-MitoDendra2 transgenic mice. The brain slices were positioned within a recording chamber and superfused with oxygenated ACSF at a flow rate of 1.5 mL/min. Optical imaging of Dendra signals were acquired using an Ultima multiphoton laser scanner (Bruker) for BX51/61 Olympus microscope with a Titanium-sapphire laser (Chameleon-Ultra2, Coherent Laser Group), equipped with a 20 X 1.0 NA water immersion objective (XLUMPLFL20XW, Olympus). The Dendra2 protein was excited at a wavelength of 900 nm, and its fluorescence was collected at 500–560 nm. Images were captured in 8-bit resolution and 4 μs dwell time, with regions of interest set at 512 x 512 pixels. The sampling rate ranged from 0.2 to 0.5 seconds per frame. All experiments were conducted at 33–35 °C.

Images were processed using the open-source software Fiji (NIH) and MATLAB (Version 8.5.0 R2015a, MathWorks). Intensity-based alignment was performed to register images at different time points. To measure mitochondrial motility velocity, the plugins KymographClear and KymographDirect (Mangeol et al., 2016) were used to generate kymographs representing moving distance versus moving duration. The number and percentage of mitochondria in different states—static, retrograde, and anterograde—were quantified and measured.

6. **Stereotaxic injection of AAV**

Three–4 months old male mice of *Pink1*$^{+/+}$and *Pink1*$^{-/-}$ were anesthetized with isoflurane (1–2%) or ketamine/xylazine (100 mg/10 mg/kg). A small craniotomy, approximately 0.8 mm in diameter, was made over the right midbrain (−3.4 mm caudal, +1.0 mm lateral). To achieve expression of mito-GCaMP6 in dopaminergic neurons, 0.1-0.2 μl of AAV-GCaMP6-mito virus (a gift from Dr. James Surmeier's lab at Northwestern University) was pressure-injected through a syringe into the midbrain at a depth of −4.2 mm ventral from the dura surface. Following the injections, the incisional wound on the skull was sealed with tissue adhesive (3M Vetbond). The mice were placed on a heating pad until

fully recovered and then returned to the isolation room. Carprofen (5 mg/kg, Sigma Aldrich) was administered intraperitoneally once per day for at least 3 days to reduce pain.

7. 2PLSM mito-GCaMP6 imaging in acute brain slices

Mitochondrial Ca^{2+} levels were measured with the mitochondrially targeted Ca^{2+}-sensitive probe mito-GCaMP6 (Protocol: dx.doi.org/10.17504/protocols.io.5jyl8pby7g2w/v1)**.** Two-three weeks after AAV virus injection, mice were prepared for coronal brain slice sectioning following transcardial perfusion with ice-cold, oxygenated cutting solution. After a recovery period of 30-45 minutes, the coronal brain slices were placed in a chamber perfused with oxygenated ACSF. To measure free Ca^{2+} levels in mitochondria, the slices were sequentially treated with the following solutions: (1) regular ACSF, (2) 500 µM EGTA + ACSF without Ca^{2+} for 30-40 minutes, (3) 500 µM EGTA + 1 µM Ionomycin + ACSF without Ca^{2+} for 30 minutes, and (4) 1 µM Ionomycin + aCSF with high Ca^{2+} (3 mM) for 20 minutes. Time series images were acquired every 5 minutes to determine the minimal and maximal fluorescence intensity. The fluorescence intensity at the end of treatment (2) was defined as the minimum fluorescence (Fmin), and the fluorescence intensity at the end of treatment (4) was defined as the maximum fluorescence (Fmax). The relative free calcium levels was calculated using the equation: (F - Fmin) / (Fmax - Fmin).

8. Western Blot

Tissues were homogenized and lysed with RIPA buffer (Millipore Sigma, R0278) supplemented with fresh protease inhibitors (Roche, 11873580001) and phosphatase inhibitors (Roche, 04906845001). The homogenate was further lysed for 1 hour at 4°C and cleared by centrifugation at 12,000 × g for 15 minutes at 4°C. The supernatants were collected, and protein concentrations were determined using a BCA assay kit (Thermo Scientific Pierce, 23227). Protein samples (30-50 µg) were separated using Mini-PROTEAN® TGX™ Precast Gels (Bio-Rad). After blocking, the blots were incubated with primary antibodies overnight at 4°C. Following washing with 1× TBST (0.1% Tween-20), the blots were incubated with secondary antibodies (1:10000, IR dye800, Li-

COR 926-32211; Alexa 680, Invitrogen, A21057) for 1 hour and visualized using the Odyssey Infrared Imager (Li-COR, 9120). The relative protein abundance was quantified using Image Studio software (Li-COR).

9. TH-Immunogold labeling and electron microscopy

Mice were perfused intracardially with freshly prepared fixatives. The fixative consisted of 3.75% acrolein and 2% paraformaldehyde (PFA) in 0.1 M phosphate buffer, pH 7.4 (PB). After fixation, brains were sectioned at 50 µm in PB using a vibratome subsequently fixed at 4°C overnight in 4% PFA/PB. Sections were treated with 50 mM glycine in 1× PBS for 30 minutes to reduce free aldehydes and rinsed extensively with PB three times. The sections were then permeabilized with Tris-buffered saline (TBS) containing 3% goat serum, 1% bovine serum albumin (BSA), and 0.04% Triton X-100 for 30 minutes. The primary mouse anti-TH antibody (#MAB5280, Millipore Sigma) was diluted 1:100 in PBS with 3% goat serum and 1% BSA. The sections were incubated with the primary antibody at 4°C for 48 hours. After washing three times (10 minutes each) with PBS, the sections were labeled with 0.8 nm gold-conjugated goat anti-mouse secondary antibody (#800.177, Aurion) diluted in a buffer containing 3% goat serum, 0.8% BSA, and 0.1% cold fish gelatin in PBS. The sections were incubated with the secondary antibody at 4°C for 48 hours. Following one wash with dilution buffer and six washes with PBS, sections were post-fixed with 2.5% glutaraldehyde in PBS. After several washes with PBS, the sections were exposed to Enhancement Conditioning Solution (ECS; #500.055, Aurion) diluted 1:10 with ddH2O, for four times at 10 minutes each. Ultra-small gold particles were enlarged using R-Gent SE-EM Silver Enhancement Reagents (#500.044, Aurion) for 150 minutes. The sections were then rinsed in ECS before being transferred to PBS. Tissue sections were transferred to PBS in Coors dishes and fixed in 1% osmium tetroxide in PB for 60 minutes on ice. After rinsing in ddH2O, the sections were sequentially dehydrated in 30%, 50%, 70%, 85%, and 95% ethanol solutions, followed by two exposures to 100% ethanol and then two exposures to acetone. Tissue sections were incubated overnight in a 1:1 mixture of epoxy resin (#14120, EMbed 812, Electron Microscopy Sciences) and acetone before being transferred to pure EMbed 812 for 3 hours (three times, 1 hour each). The sections were then embedded in

EMbed 812 and polymerized for 24 hours at 65°C. Plastic blocks were trimmed and sectioned with a Leica ultramicrotome (EM UC7, Leica) equipped with a 35° diamond knife (Diatome). Serial ultrathin sections (75 nm) were collected on single-slot formvar-coated copper grids. After post-staining with uranyl acetate and lead citrate, the grids were examined under a transmission electron microscope (Tecnai G^2 Spirit BioTWIN, FEI) equipped with a digital camera (Orius 832, Gatan) at 120kV.

10. Data and Statistical Analysis

Data were presented as mean ± SEM unless otherwise specified. Statistical analyses were conducted using Prism 9.0 (GraphPad), including the Mann–Whitney test, Wilcoxon test, t-test, and one-way or two-way ANOVA followed by the Bonferroni post-test. Differences were considered statistically significant when $P < 0.05$. Statistical analysis was based on the number of slices or experiments unless otherwise noted. "N" denotes the number of mice, and "n" denotes the number of experiments.

Antibodies and reagents

Antibody	Source	Dilution	Catalog number
Anti-Tyrosine Hydroxylase	rabbit	1:5000 (IF)	Pel-Freez, P40101-0
Anti-Tyrosine Hydroxylase	mouse	1:500 (IF)	Millipore, MAB5280
Anti-Kinesin heavy chain	mouse	1:500 (WB)	Millipore, MAB1614
Anti-Dynein medium chain	mouse	1:1000 (WB)	Millipore, MAB1618
Anti-Miro1	rabbit	1:1000 (WB)	Antibodies_online, ABIN635090
MAPK Family Antibody	rabbit	1:1000 (WB)	Cell signaling,9926
Phospho-MAPK Family Antibody	rabbit	1:1000 (WB)	Cell signaling,9910
Anti-MnSOD	rabbit	1:1000 (WB)	Abcam, ab68155
Anti-MnSOD	rabbit	1:100 (IF)	Abcam, ab13534
Anti-β-actin	rabbit	1:1000 (WB)	Cell signaling, 4970T
DyLight 594 Antibody	Goat anti-rabbit	1:500 (IF)	Invitrogen,35560
Alexa Fluor 488nm	Goat anti-mouse	1:1000 (IF)	Invitrogen, A-11029
Alexa Fluor 594nm	Goat anti-rabbit	1:1000 (IF)	Invitrogen, A-11012
IRDye® 800CW	Goat anti-rabbit	1:5000 (WB)	Li-COR, 926-32211
IRDye® 680RD	Goat anti-mouse	1:5000 (WB)	Li-COR, 926-68070
A23187			Sigma-Aldrich, C7522
CGP37157			Sigma-Aldrich, C8874
Menadione			Sigma-Aldrich, M5625

Ionomycin	Sigma-Aldrich, I3909

Acknowledgements

This work was supported by Thomas Jefferson University, Peking University School of Life Sciences and The University of Georgia. The authors wish to thank Dr. Ying-Chun Hu, Zhen-Yang Kong, and Hong-Zhang Zhou for their expert technical assistance with EM sample preparation and image analysis at the Core Facilities of the School of Life Sciences, Peking University. Additionally, we thank Dr. D. James Surmeier for providing the AAV virus.

Competing interests

The authors declare no conflict of interest.

Figure legends

Figure1. Generation and characterization of TH-Mito-Dendra2 (MD) BAC transgenic mouse

(A) Depiction of the TH-MitoDendra2 BAC construct. To modify RPCI23-350E13 BAC, a targeting cassette was generated with A arm, B arm and mitochondrial-targeting dendra2 insert. The mito-dentra2 and *Th* gene exon1 share the same initiation ATG codon. A and B represent the homologous recombination regions. MTS: mitochondrial targeting sequence.

(B) A coronal section of TH-Mito-Dendra2 (MD) BAC transgenic mouse brains shows the histological overview of Mito-Dentra2 expression pattern. Tyrosine hydroxylase (TH) signal (red) co-localizes with Mito-Dentra2 fluorescence (green) in midbrain areas.

(C) Mito-Dendra2 (green) expressing cells are all TH (red) immunoreactive in the substantia nigra (SN).

(D) Mito-Dendra2 (green) expressing cells are all TH (red) immunoreactive in the ventral tegmental area (VTA).

(E) A sagittal section of TH-MitoDendra2 BAC mouse brain showing continuous and intact nigrostriatal axonal projection of dopaminergic neurons.

(F) MitoDendra2 is localized in mitochondria, as labeled with MitoTracker, in the striatum of TH-mitodendra2-BAC transgenic mice

Figure 2. Investigation of mitochondrial movement in acute brain slices using two-photon laser microscopy (2PLSM)

(A) Schematic illustration of mitochondrial trafficking imaging in acute brain slices.
(B) Image sequences of mitochondrial trafficking. B1-B6 represent images of mitochondria moving at the different time points: 0, 5, 10, 15, 20 and 25 seconds, respectively. White circles 1 and 2 denote the anterograde movement of mitochondria, blue circle 3 denotes the retrograde movement of mitochondria.
(C) Kymograph generation and mitochondria trafficking measurement. C1: Representative image of mitochondria expressing Dendra2 protein. C2: Maximum intensity projection of a series of mitochondrial trafficking images. C3: Pseudo color map of panel C2 to facilitate outlining the trace of mitochondrial movement. C4: Kymograph map generated from the images, showing anterograde, retrograde, and static traces.

Figure 3. Age-dependent mitochondrial axonal transport deficits in *Pink1*$^{-/-}$ mice

(A) Representative images of the mitochondrial trafficking imaging window at the imaging start point. A1-A2 show the images of *Pink1*$^{+/+}$ and *Pink1*$^{-/-}$ mice at 2-4 months old, respectively. A3-A4 show the images of *Pink1*$^{+/+}$ and *Pink1*$^{-/-}$ mice at 5-7 months old, respectively. A5-A6 show the images of *Pink1*$^{+/+}$ and *Pink1*$^{-/-}$ mice older than 10 months, respectively.
(B) Representative kymograph showing different mitochondrial trafficking statuses. Red lines indicate the anterograde trace of mitochondrial movement, green lines indicate the retrograde movement, and blue lines represent static mitochondria.
(C) Quantitative summary of different mitochondrial moving statuses in 2-4 months old *Pink1*$^{+/+}$ and *Pink1*$^{-/-}$ mice. Data are presented as mean ± SEM, and the p-value was calculated using the Student's t-test. *Pink1*$^{+/+}$: N=3, n=8; *Pink1*$^{-/-}$: N=3, n=12.
(D) Quantitative summary of different mitochondrial moving statuses in 5-7 months old *Pink1*$^{+/+}$ and *Pink1*$^{-/-}$ mice. Data are presented as mean ± SEM, and the p-value was calculated using the Student's t-test. **$p<0.01$, **** $p<0.0001$. *Pink1*$^{+/+}$: N=3, n=10; *Pink1*$^{-/-}$: N=5, n=12.
(E) Box plot of anterograde (left) and retrograde (right) velocity (min to max) of different genotypes in 5-7 months old mice. The p-value was calculated using unpaired t-test. *$p<0.05$.
(F) Quantitative summary of different mitochondrial moving statuses in *Pink1*$^{+/+}$ and *Pink1*$^{-/-}$ mice older than 10 months. Data are presented as mean ± SEM, and the p-value was calculated using the Student's t-test. *$p<0.05$, **$p<0.01$. *Pink1*$^{+/+}$: N=3, n=5; *Pink1*$^{-/-}$: N=4, n=9.
(G) Box plot of anterograde (left) and retrograde (right) velocity (min to max) of different genotypes older than 10 months. The p-value was calculated using unpaired t-test.

Figure 4. Mitochondrial calcium elevation and transport deficits in acute brain slices

(A) Representative images of TH-mito-GCaMP6 imaging in approximately 3-month-old *Pink1*$^{+/+}$ (upper row) and *Pink1*$^{-/-}$ mice (lower row). The left column shows the original mitochondrial [Ca^{2+}] under regular aCSF. Fluorescence signals decrease after 20 minutes of 0 mM Ca^{2+} (containing 500 µM EGTA) aCSF perfusion (middle column). After 3 mM Ca^{2+} aCSF perfusion for 30 minutes, the mito-GCaMP6 fluorescence signal overshoots and reaches the highest level (right column).
(B) Quantitative results for mitochondrial [Ca^{2+}] in *Pink1*$^{+/+}$ (N=3, n=8) and *Pink1*$^{-/-}$ (N=3, n=12) mice. Data are presented as mean ± SEM, and the p-value is calculated using unpaired t-test, ****p<0.0001.
(C) Representative captures and kymographs before (C1 and C3) and after (C2 and C4) 5 µM CGP37157 incubation for 2 hours.
(D) Quantification of different mitochondrial moving statuses after 5 µM CGP37157 incubation. Data are presented as mean ± SEM, and the p-value is calculated using unpaired t-test, *p<0.05, **p<0.01. Ctrl: N=3, n=6; CGP37157: N=3, n=7.
(E) Box plot shows anterograde (left), and retrograde (right) velocity remain unchanged in the CGP37157 treatment group compared to the control group. The p-value is calculated using unpaired t-test.

Figure 5: NCLX inhibition-induced mitochondrial Ca^{2+} overload leading to enhanced oxidative levels

(A-B) Representative images of SNc dopaminergic neurons expressing roEGFP. Neurons were excited at 900 nm (reduced state) and 800 nm (oxidized state) under different incubation conditions: regular aCSF (A1-A2) and aCSF with 10 µM CGP37157 **(**B1-B2). (C**)** Elevated Oxidative levels after treatment with 10 µM CGP37157 for 60 minutes. Data are presented as mean ± SEM. P-values were calculated using unpaired t-test. ***p<0.001, Ctrl: n=20; CGP37157: n=19 (n represents the number of neurons).

Figure 6: Reduced mitochondrial anterograde movement by ROS elevation

(A) Representative images of mitochondrial trafficking under different incubation conditions at the start point: Regular aCSF (A1); 0.2% DMSO in aCSF (A2); 50 µM menadione (MED) in aCSF (A3).
(B) Representative kymographs showing mitochondrial trafficking status after different treatments: Regular aCSF (B1); 200 µL DMSO in aCSF (B2); 50 µM menadione (MED) in aCSF (B3).
(C) Percentage quantification of mitochondrial movement status under different incubation conditions. Data are presented as mean ± SEM. P-values were calculated using two-way ANOVA. *p<0.05, **p<0.01, ****p<0.0001. Regular aCSF control: N=3, n=8; DMSO control: N=3, n=6; menadione: N=3, n=4.
(D) Effect of menadione treatment on mitochondrial movement velocity (Anterograde: left, Retrograde: right). P-values were calculated using one-way ANOVA.
(E) Immunoblot showing MnSOD expression levels in striatum (left) and substantia nigra (right) of 5-7 months old *Pink1*$^{+/+}$ and *Pink1*$^{-/-}$ mice.

(F) Quantification of MnSOD expression levels in striatum (left) and substantia nigra (right) of 5-7 months old *Pink1*$^{+/+}$ and *Pink1*$^{-/-}$ mice. P-values were calculated using unpaired t-test. **p<0.01, *p<0.05.
(G) TH immunofluorescence staining of dopaminergic neurons in the nigrostriatal region of 5-7 months old *Pink1*$^{+/+}$ (G1) and *Pink1*$^{-/-}$ mice (G2).
(H) MnSOD immunofluorescence staining in the substantia nigra striatum region of -7 months old *Pink1*$^{+/+}$ (H1) and *Pink1*$^{-/-}$ mice (H2).
(I) Quantification of relative MnSOD fluorescence intensity in dopaminergic neurons of 5-7 months old *Pink1*$^{+/+}$ mice and *Pink1*$^{-/-}$ mice. P-values were calculated using unpaired t-test. ****p<0.0001.

Figure 7: p38 MAPK pathway hyperactivation by loss of *Pink1* and improved mitochondrial motility in *Pink1*$^{-/-}$ mice by p38 inhibition.

(A) Immunoblot showing expression levels of phospho-p38 and total p38 in striatum (left) and substantia nigra (right) of 6-7 months old *Pink1*$^{+/+}$ and *Pink1*$^{-/-}$ mice.
(B) Quantification of phospho-p38 and total p38 expression levels in striatum (left) and substantia nigra (right). P-values were calculated using unpaired t-test. **p<0.01, ****p<0.0001.
(C) Representative images of mitochondrial trafficking under different incubation conditions at the start point: Regular aCSF (C1); 50 μM p38 inhibitor (SB202190) in aCSF (C2).
(D) Representative kymographs showing mitochondrial trafficking status: Regular aCSF (D1); 50 μM SB202190 incubation (D2).
(E) Percentage quantification of mitochondrial movement status after SB202190 incubation. Data are presented as mean ± SEM. P-values were calculated using two-way ANOVA. **p<0.01, ****p<0.0001. Regular aCSF control: N=3, n=6; SB202190: N=3, n=7.
(F) Effect of SB202190 treatment on mitochondrial movement velocity. P-values were calculated using unpaired t-test.

Figure 8: Defective Mitochondrial quantity and quality in dopamine neuron terminals in *Pink1*$^{-/-}$ mice.

(A-B) TH immunogold electron microscopy (EM) showing mitochondrial morphology in dopaminergic terminals: Representative images from *Pink1*$^{+/+}$ (C) and *Pink1*$^{-/-}$ mice. Blue arrows: TH-positive signals in dopamine terminals. Red arrows: Mitochondria within or around dopamine terminals.
(C) Quantification of mitochondrial status in dopaminergic terminals and other regions of the striatum in *Pink1*$^{+/+}$ and *Pink1*$^{-/-}$ mice. P-values were calculated using paired t-test. **p<0.01, N=5.
(D) Quantification of mitochondrial aspect ratio in dopaminergic terminals of *Pink1*$^{+/+}$ and *Pink1*$^{-/-}$ mice. P-values were calculated using unpaired t-test. ***p<0.001, N=5.

(E) Mechanistic hypothesis: *Pink1* gene deletion causes defects in mitochondrial axonal transport in dopaminergic neurons.

References

Berth SH, Lloyd TE. 2023. Disruption of axonal transport in neurodegeneration. *J Clin Invest* **133**. doi:10.1172/JCI168554

Brady ST, Morfini GA. 2017. Regulation of motor proteins, axonal transport deficits and adult-onset neurodegenerative diseases. *Neurobiol Dis* **105**:273–282. doi:10.1016/J.NBD.2017.04.010

Candas D, Li JJ. 2014. MnSOD in Oxidative Stress Response-Potential Regulation via Mitochondrial Protein Influx. *Antioxid Redox Signal* **20**:1599. doi:10.1089/ARS.2013.5305

Das Banerjee T, Dagda RKRY, Dagda M, Chu CT, Rice M, Vazquez-Mayorga E, Dagda RKRY. 2017. PINK1 regulates mitochondrial trafficking in dendrites of cortical neurons through mitochondrial PKA. *J Neurochem* **142**:545–559. doi:10.1111/jnc.14083

Debattisti V, Gerencser AA, Saotome M, Das S, Hajnóczky G. 2017. ROS Control Mitochondrial Motility through p38 and the Motor Adaptor Miro/Trak. *Cell Rep* **21**:1667–1680. doi:10.1016/j.celrep.2017.10.060

Exner N, Lutz AK, Haass C, Winklhofer KF. 2012. Mitochondrial dysfunction in Parkinson′s disease: Molecular mechanisms and pathophysiological consequences. *EMBO J* **31**:3038–3062. doi:10.1038/emboj.2012.170

Giorgi C, Marchi S, Pinton P. 2018. The machineries, regulation and cellular functions of mitochondrial calcium. *Nat Rev Mol Cell Biol 2018 1911* **19**:713–730. doi:10.1038/s41580-018-0052-8

Gong S, Yang XW, Li C, Heintz N. 2002. Highly Efficient Modification of Bacterial Artificial Chromosomes (BACs) Using Novel Shuttle Vectors Containing the R6Kγ Origin of Replication. *Genome Res* **12**:1992–1998. doi:10.1101/GR.476202

Haaxma CA, Bloem BR, Borm GF, Oyen WJG, Leenders KL, Eshuis S, Booij J, Dluzen DE, Horstink MWIM. 2007. Gender differences in Parkinson’s disease. *J Neurol Neurosurg Psychiatry* **78**:819–824. doi:10.1136/jnnp.2006.103788

Kostic M, Ludtmann MHR, Bading H, Hershfinkel M, Steer E, Chu CT, Abramov AY, Sekler I. 2015. PKA Phosphorylation of NCLX Reverses Mitochondrial Calcium Overload and Depolarization, Promoting Survival of PINK1-Deficient Dopaminergic Neurons. *Cell Rep* **13**:376–386. doi:10.1016/j.celrep.2015.08.079

Liu S, Sawada T, Lee S, Yu W, Silverio G, Alapatt P, Millan I, Shen A, Saxton W, Kanao T,

Takahashi R, Hattori N, Imai Y, Lu B. 2012. Parkinson's Disease–Associated Kinase PINK1 Regulates Miro Protein Level and Axonal Transport of Mitochondria. *PLoS Genet* **8**:e1002537. doi:10.1371/journal.pgen.1002537

Liu W, Acín-Peréz R, Geghman KD, Manfredi G, Lu B, Li C. 2011. Pink1 regulates the oxidative phosphorylation machinery via mitochondrial fission. *Proc Natl Acad Sci U S A* **108**:12920–12924. doi:10.1073/pnas.1107332108

Malpartida AB, Williamson M, Narendra DP, Wade-Martins R, Ryan BJ. 2020. Mitochondrial Dysfunction and Mitophagy in Parkinson's Disease: From Mechanism to Therapy. *Trends Biochem Sci* **0**:1–15. doi:10.1016/j.tibs.2020.11.007

Mangeol P, Prevo B, Peterman EJG. 2016. KymographClear and KymographDirect: Two tools for the automated quantitative analysis of molecular and cellular dynamics using kymographs. *Mol Biol Cell* **27**:1948–1957. doi:10.1091/mbc.E15-06-0404

Morfini GA, Bosco DA, Brown H, Gatto R, Kaminska A, Song Y, Molla L, Baker L, Marangoni MN, Berth S, Tavassoli E, Bagnato C, Tiwari A, Hayward LJ, Pigino GF, Watterson DM, Huang CF, Banker G, Brown RH, Brady ST. 2013. Inhibition of Fast Axonal Transport by Pathogenic SOD1 Involves Activation of p38 MAP Kinase. *PLoS One* **8**:e65235. doi:10.1371/JOURNAL.PONE.0065235

Padzik A, Deshpande P, Hollos P, Franker M, Rannikko EH, Cai D, Prus P, Mågård M, Westerlund N, Verhey KJ, James P, Hoogenraad CC, Coffey ET. 2016. KIF5C S176 Phosphorylation Regulates Microtubule Binding and Transport Efficiency in Mammalian Neurons. *Front Cell Neurosci* **10**. doi:10.3389/FNCEL.2016.00057

Park JS, Davis RL, Sue CM. 2018. Mitochondrial Dysfunction in Parkinson's Disease: New Mechanistic Insights and Therapeutic Perspectives. *Curr Neurol Neurosci Rep*. doi:10.1007/s11910-018-0829-3

Peng TI, Jou MJ. 2010. Oxidative stress caused by mitochondrial calcium overload. *Ann N Y Acad Sci* **1201**:183–188. doi:10.1111/J.1749-6632.2010.05634.X

Poewe W, Seppi K, Tanner CM, Halliday GM, Brundin P, Volkmann J, Schrag AE, Lang AE. 2017. Parkinson disease. *Nat Rev Dis Prim* **3**:1–21. doi:10.1038/nrdp.2017.13

Pryde KR, Smith HL, Chau KY, Schapira AHV. 2016. PINK1 disables the anti-fission machinery to segregate damaged mitochondria for mitophagy. *J Cell Biol* **213**:163–171. doi:10.1083/jcb.201509003

Ruiz A, Alberdi E, Matute C. 2014. CGP37157, an inhibitor of the mitochondrial Na+/Ca2+ exchanger, protects neurons from excitotoxicity by blocking voltage-gated Ca2+ channels **5**:e1156–e1156.

Santulli G, Xie W, Reiken SR, Marks AR. 2015. Mitochondrial calcium overload is a key determinant in heart failure. *Proc Natl Acad Sci U S A* **112**:11389–11394. doi:10.1073/PNAS.1513047112/SUPPL_FILE/PNAS.201513047SI.PDF

Schwarz TL. 2013. Mitochondrial trafficking in neurons. *Cold Spring Harb Perspect Biol* **5**. doi:10.1101/cshperspect.a011304

Sheng ZH. 2014. Mitochondrial trafficking and anchoring in neurons: New insight and implications. *J Cell Biol*. doi:10.1083/jcb.201312123

Vilain S, Esposito G, Haddad D, Schaap O, Dobreva MP, Vos M, Van Meensel S, Morais VA, De Strooper B, Verstreken P. 2012. The Yeast Complex I Equivalent NADH Dehydrogenase Rescues pink1 Mutants. *PLoS Genet* **8**:e1002456. doi:10.1371/journal.pgen.1002456

Wang X, Schwarz TL. 2009. The Mechanism of Ca2+-Dependent Regulation of Kinesin-Mediated Mitochondrial Motility. *Cell* **136**:163–174. doi:10.1016/j.cell.2008.11.046

Wang X, Winter D, Ashrafi G, Schlehe J, Liang Wong Y, Selkoe D, Rice S, Steen J, Lavoie MJ, Schwarz TL, Wong YL, Selkoe D, Rice S, Steen J, Lavoie MJ, Schwarz TL. 2011. PINK1 and Parkin target miro for phosphorylation and degradation to arrest mitochondrial motility. *Cell* **147**:893–906. doi:10.1016/j.cell.2011.10.018

Weihofen A, Thomas KJ, Ostaszewski BL, Cookson MR, Selkoe DJ. 2009. Pink1 forms a multiprotein complex with miro and milton, linking Pink1 function to mitochondrial trafficking. *Biochemistry* **48**:2045–2052. doi:10.1021/bi8019178

Winklhofer KF, Haass C. 2010. Mitochondrial dysfunction in Parkinson's disease. *Biochim Biophys Acta - Mol Basis Dis*. doi:10.1016/j.bbadis.2009.08.013

Zhi L, Qin Q, Muqeem T, Seifert EL, Liu W, Zheng S, Li C, Zhang H. 2019. Loss of PINK1 causes age-dependent decrease of dopamine release and mitochondrial dysfunction HHS Public Access. *Neurobiol Aging* **75**:1–10. doi:10.1016/j.neurobiolaging.2018.10.025

Zhu XH, Qiao H, Du F, Xiong Q, Liu X, Zhang X, Ugurbil K, Chen W. 2012. Quantitative imaging of energy expenditure in human brain. *Neuroimage* **60**:2107–2117. doi:10.1016/j.neuroimage.2012.02.013

Zhao J *et al.* Figure 1.

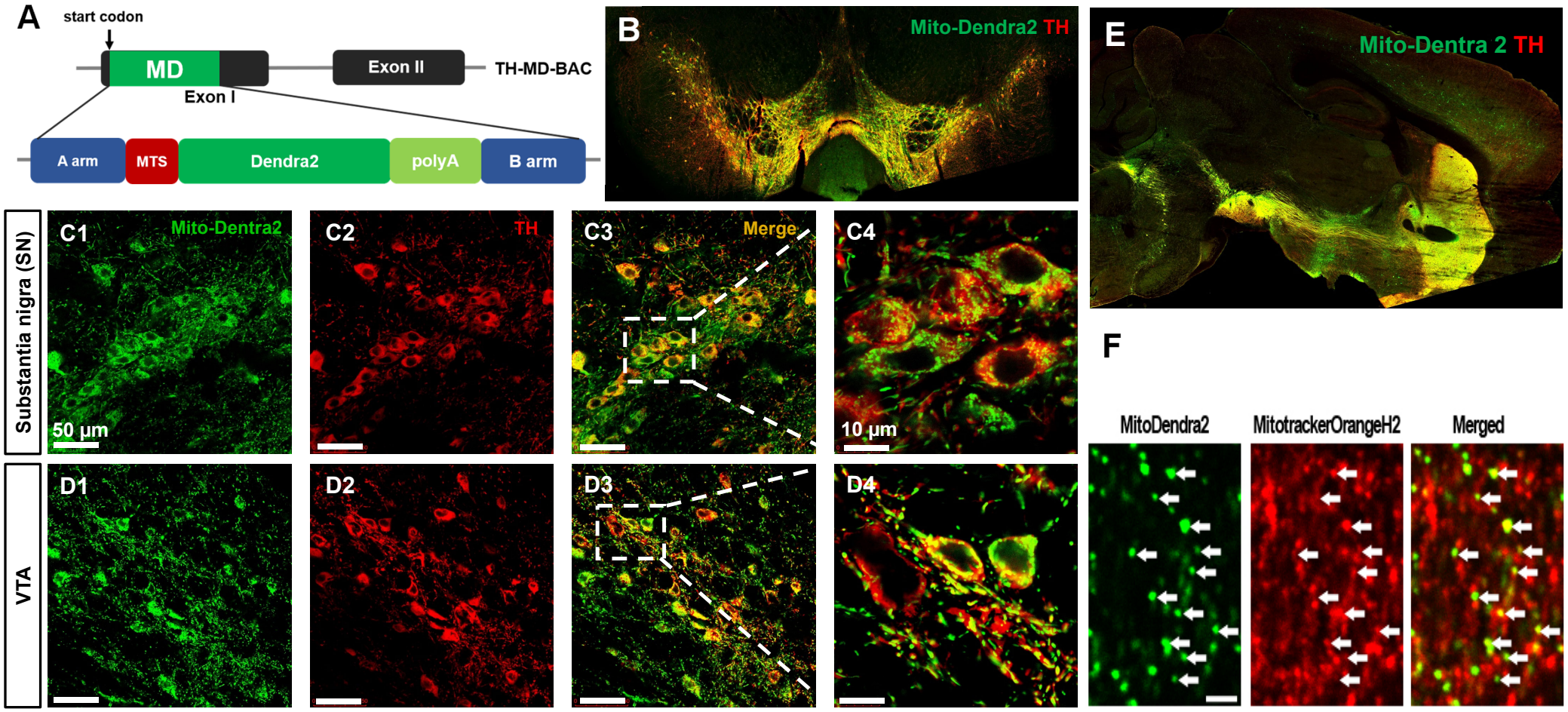

Zhao J *et al.* Figure 2.

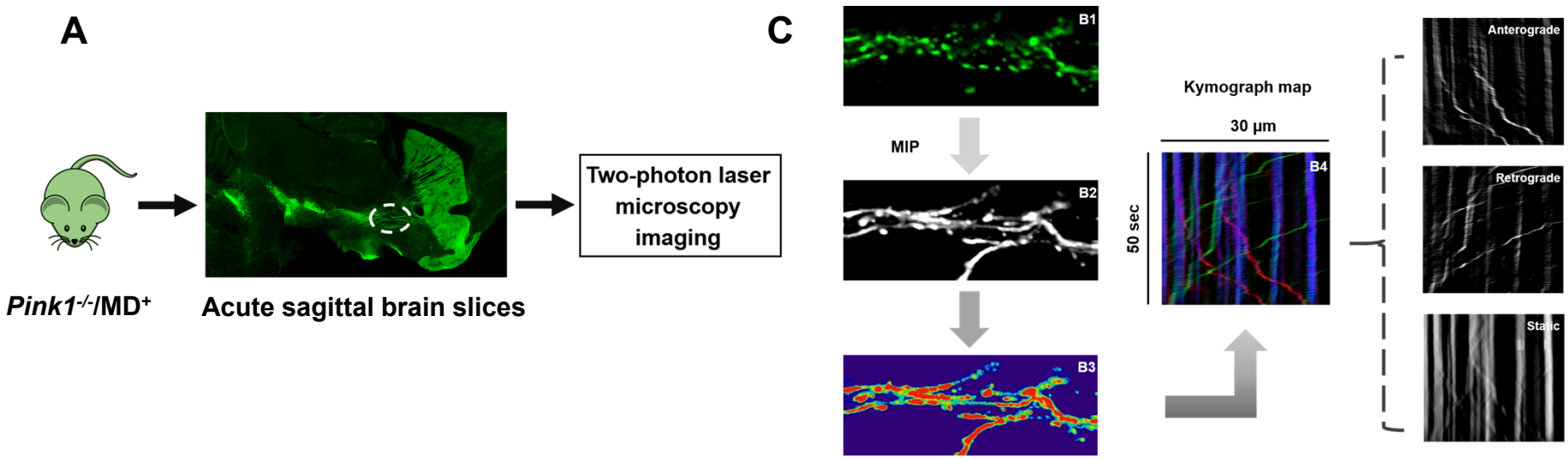

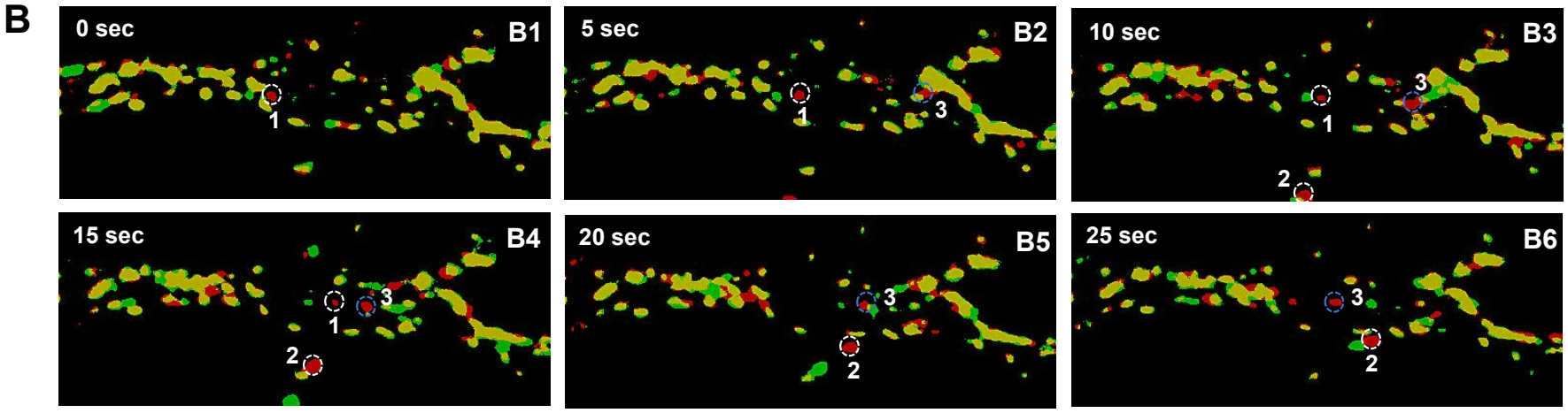

Zhao J *et al.* Figure 3

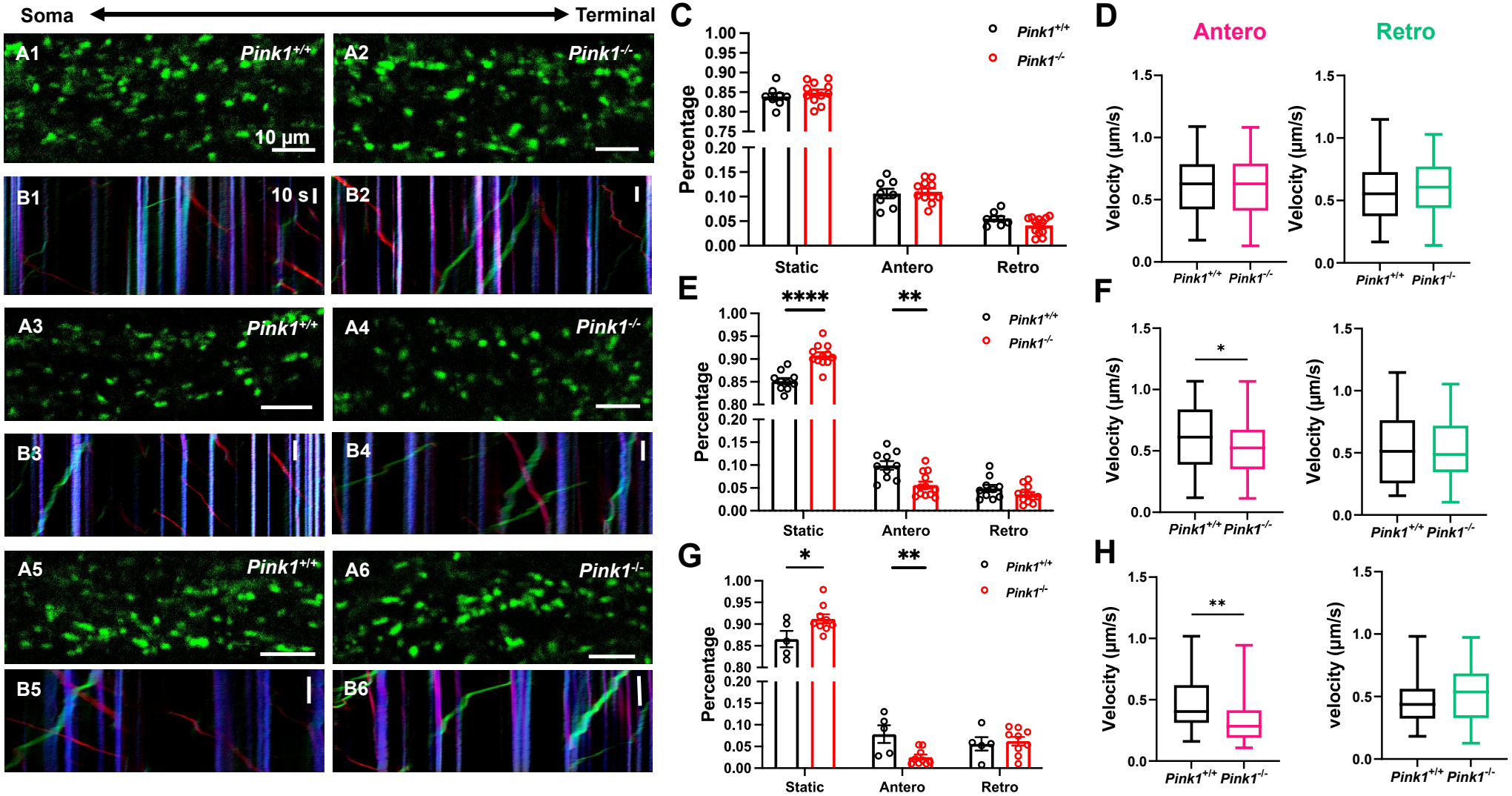

Zhao J *et al.* Figure 4.

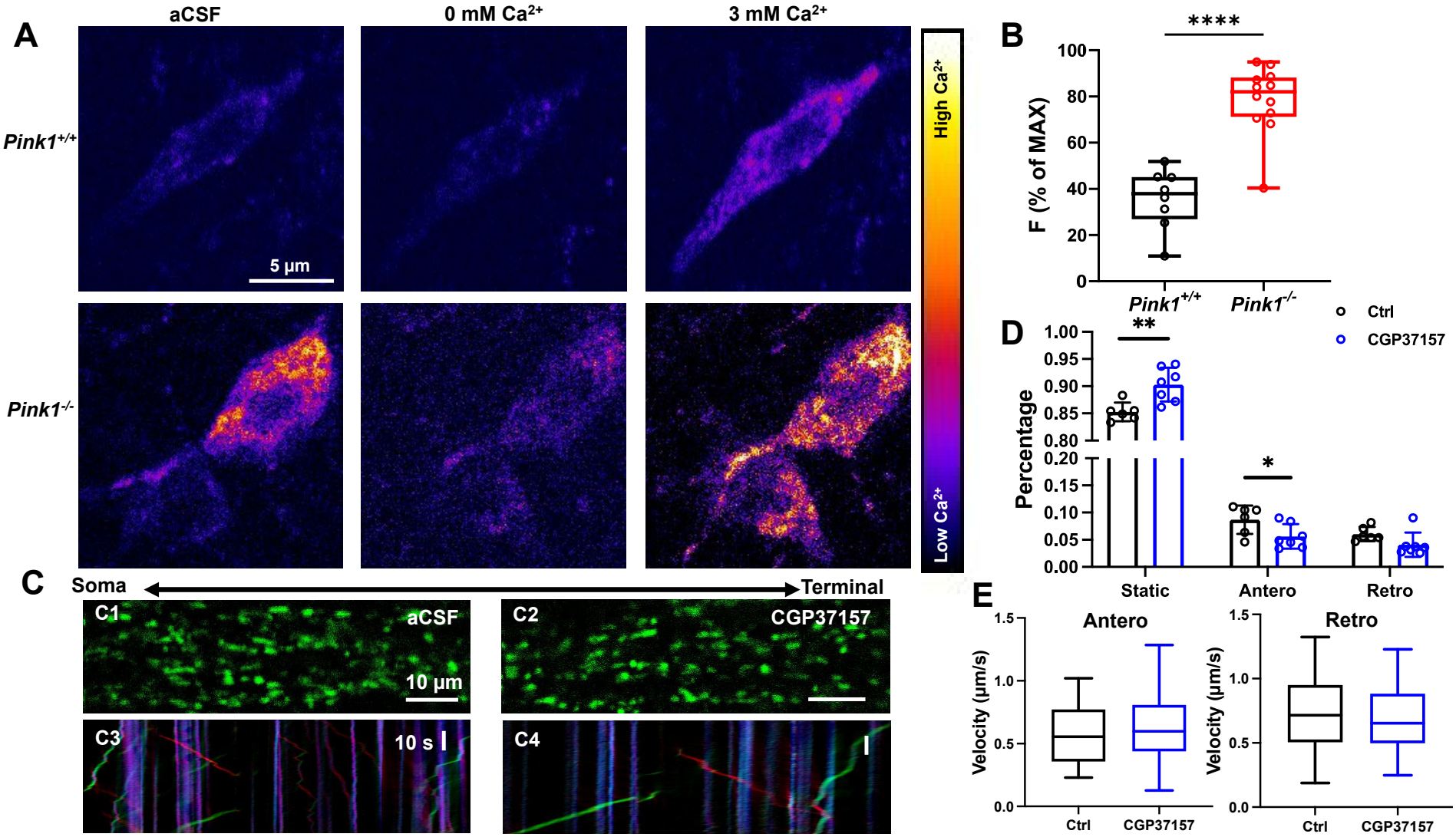

Zhao J *et al.* Figure 5.

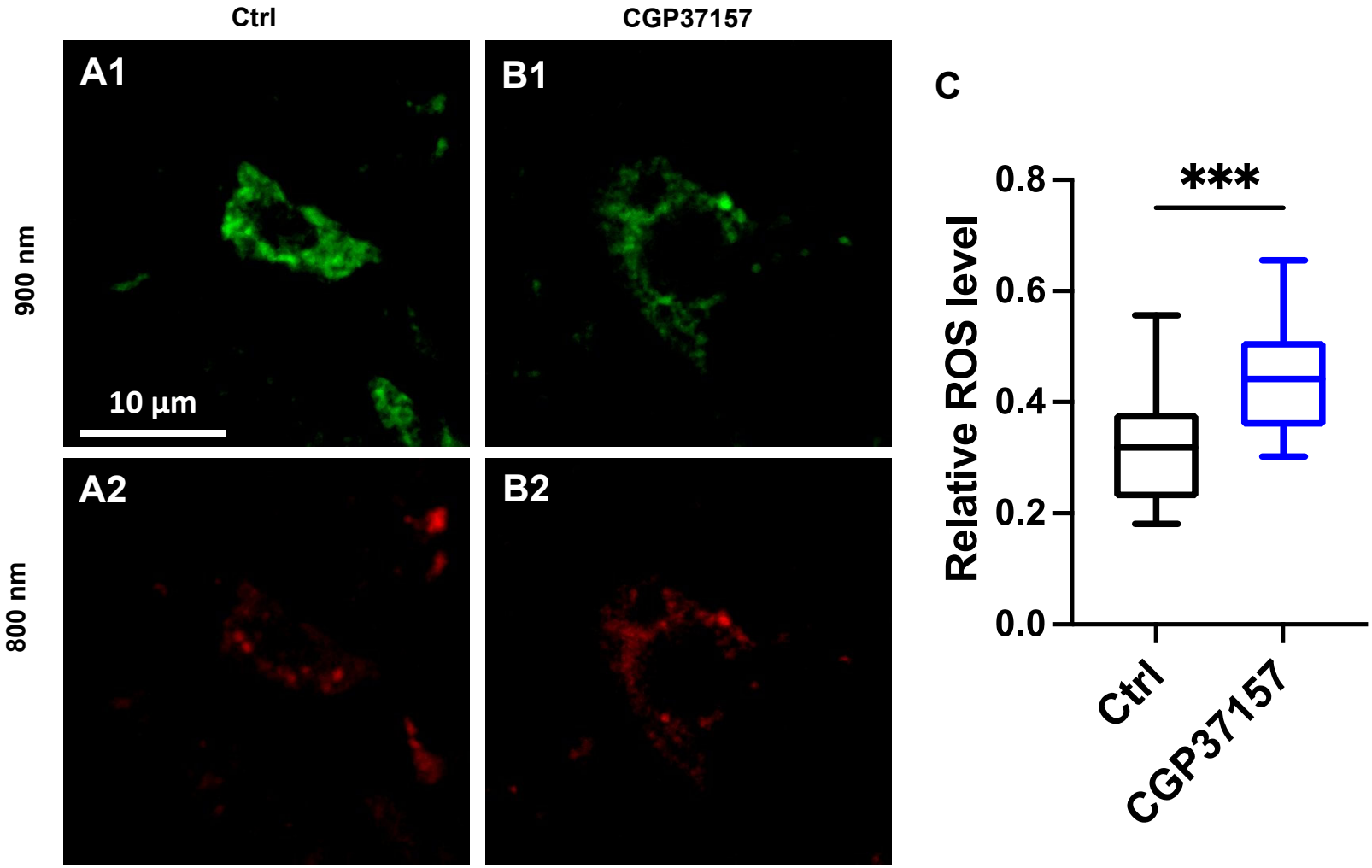

Zhao J *et al.* Figure 6.

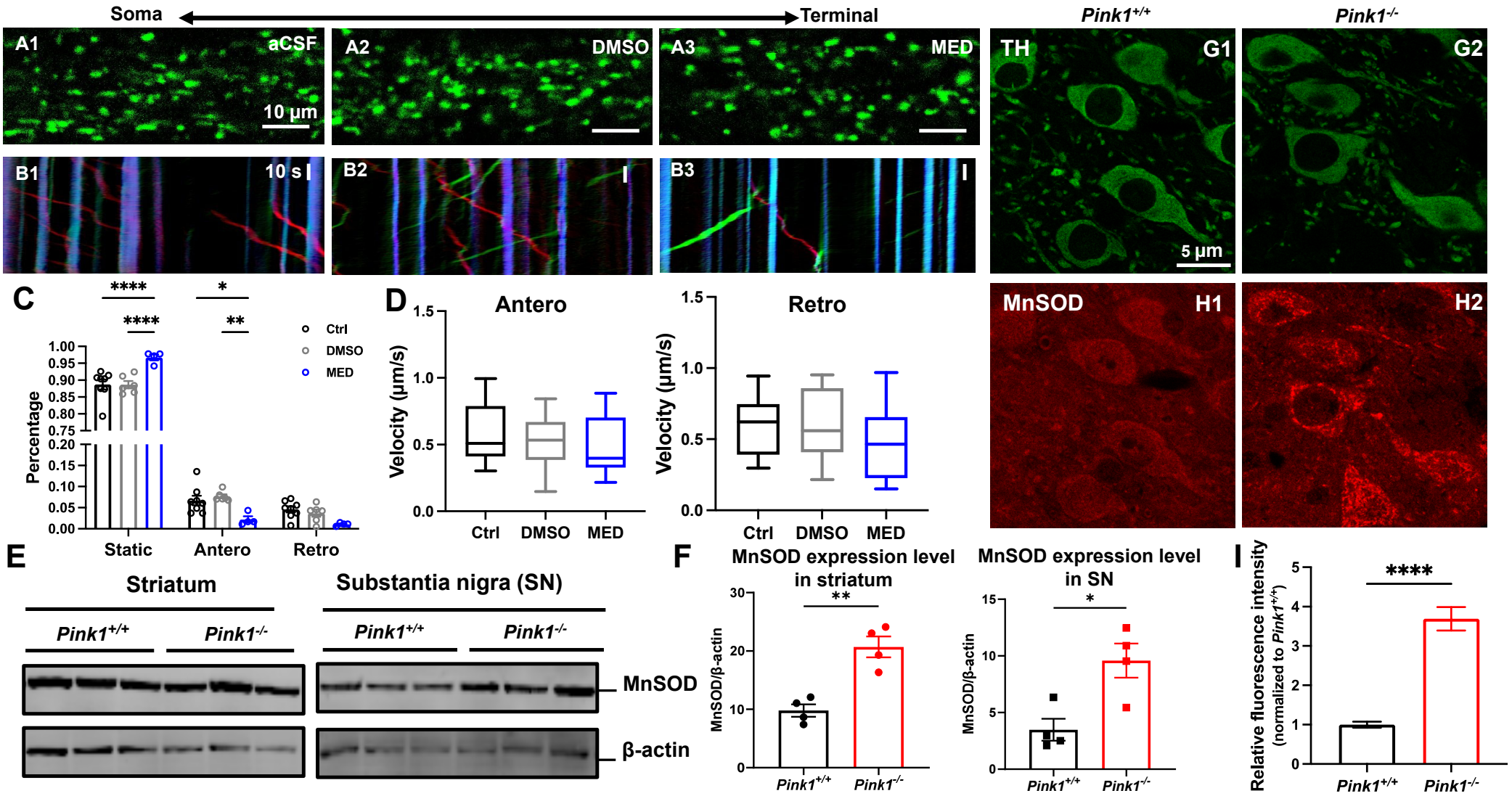

Zhao J *et al.* Figure 7.

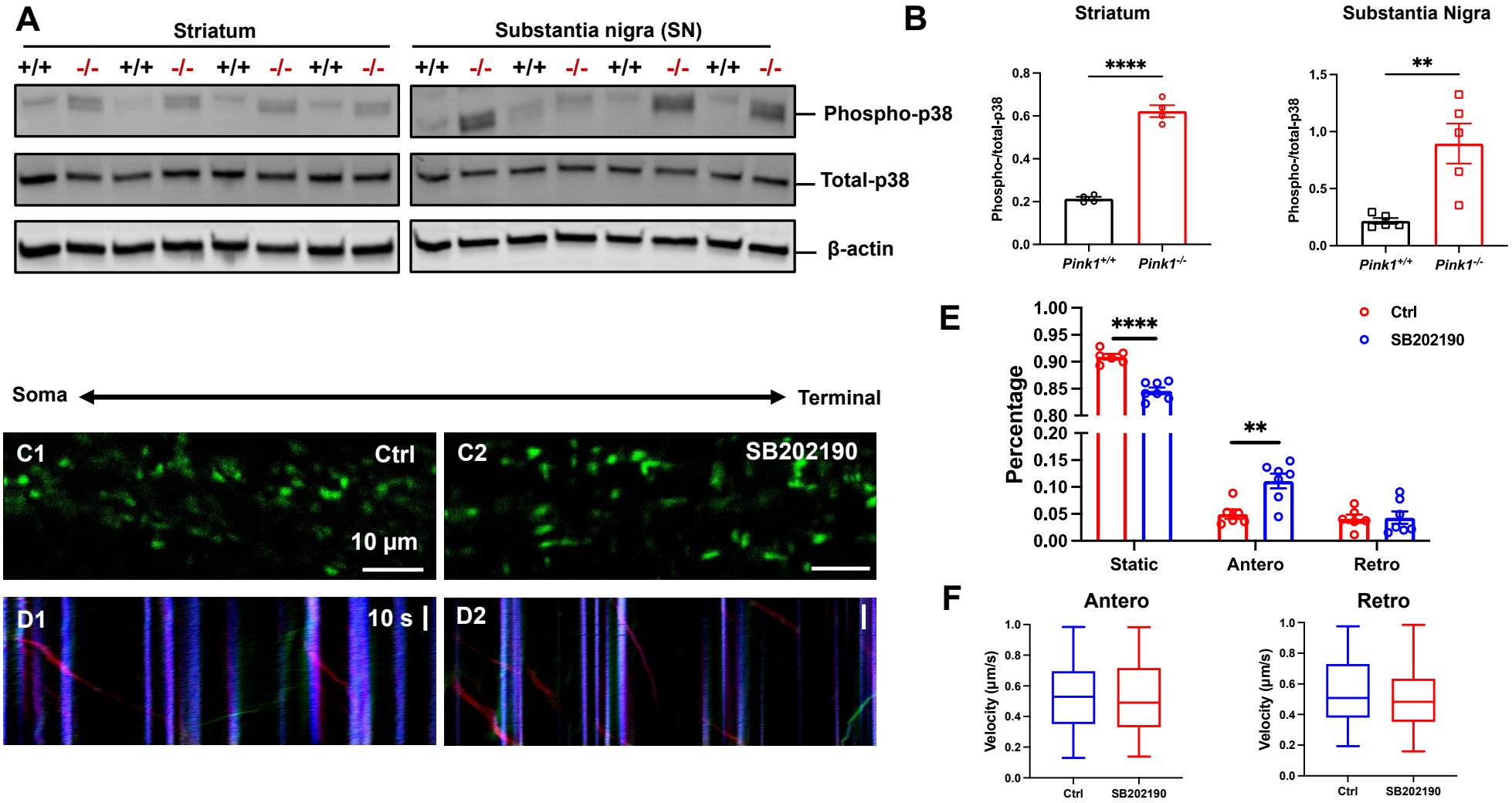
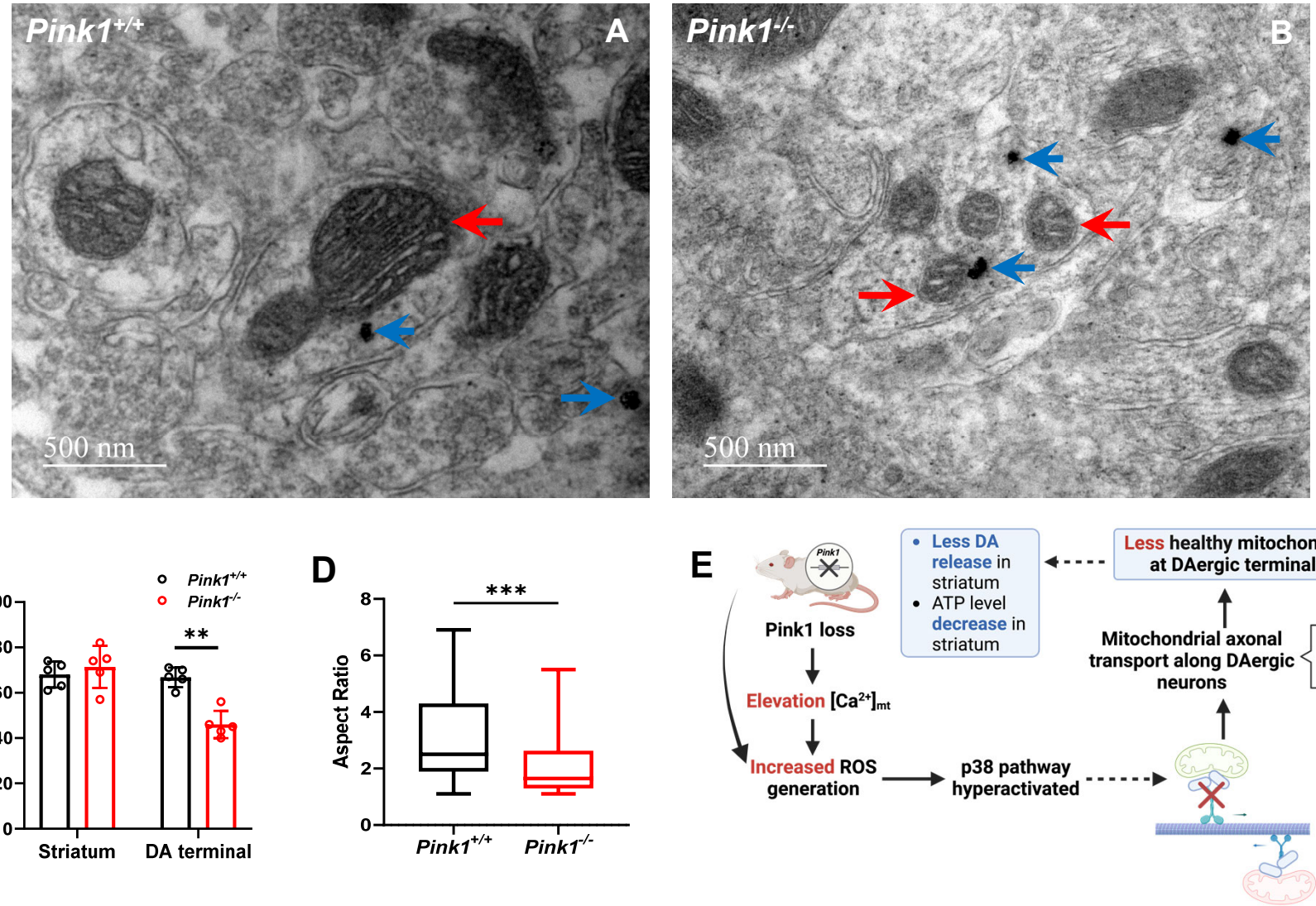
Zhao J *et al.* Figure 8.